nature physics

ARTICLES

https://doi.org/10.1038/s41567-022-01574-3

Check for updates

# Interaction-driven giant thermopower in magic-angle twisted bilayer graphene

Arup Kumar Paul[1,4], Ayan Ghosh[1,4], Souvik Chakraborty[1,4], Ujjal Roy[1], Ranit Dutta[1], K. Watanabe[2], T. Taniguchi[2], Animesh Panda[1], Adhip Agarwala[3], Subroto Mukerjee[1], Sumilan Banerjee[1] and Anindya Das[1]✉

**Magic-angle twisted bilayer graphene has proved to be a fascinating platform to realize and study emergent quantum phases arising from the strong correlations in its flat bands. Thermal transport phenomena, such as thermopower, are sensitive to the particle–hole asymmetry, making them a crucial tool to probe the underlying electronic structure of this material. Here we have carried out thermopower measurements of magic-angle twisted bilayer graphene as a function of carrier density, temperature and magnetic field. We report the observation of an unusually large thermopower reaching a value of the order of 100 μV K$^{-1}$ at a low temperature of 1 K. The thermopower exhibits peak-like features that violate the Mott formula in close correspondence to the resistance peaks appearing around the integer filling of the moiré bands, including the Dirac point. We show that the large thermopower peaks and their associated behaviour arise from the emergent highly particle–hole-asymmetric electronic structure, due to the sequential filling of the moiré flat bands and the associated recovery of Dirac-like physics. Furthermore, the thermopower shows an anomalous peak around the superconducting transition, which points towards the possible role of superconducting fluctuations in magic-angle twisted bilayer graphene.**

Interactions in many-body systems lead to various complex emergent quantum phenomena such as superconductivity, magnetism and correlated insulating phases. Understanding these many-body quantum phenomena and utilizing their various applicabilities remains a key focus of condensed matter research. For this reason, magic-angle twisted bilayer graphene (MATBLG) is a promising material with its flat-band[1–3] induced plethora of exotic states such as correlated insulator[2,4–7], superconductivity[3,4,6–9], ferromagnetism[10], Chern insulator[5,11–15], quantum anomalous Hall effect[16], nematicity[17,18] and Pomeranchuk effect[19,20]. The discovery of these emergent quantum phases, together with its easy tunability using a variety of experimental methods, makes MATBLG an unprecedented platform to probe the role of interactions in its unique electronic band structure and further the search for novel electronic properties with technological applicability. In this direction, primarily electrical transport and local spectroscopic measurements have been utilized to probe and study the nature of the various symmetry-breaking electronic states[21–25]. Notably, recent measurements of local compressibility[25] and scanning tunnelling microscopy[24] have revealed that the Fermi surface of MATBLG is highly malleable and undergoes interaction-driven quantum phase transitions at integer fillings of the moiré lattice. The key finding is the resetting of the Fermi surface with a strongly particle–hole-asymmetric density of states around the integer fillings via a cascade of Dirac revival transitions[24,25]. However, unambiguous signatures of the above phenomena in global transport measurement are still lacking. Some signature is observed in Hall measurement[5,9], where the Hall carrier density suddenly resets from a finite value to zero without changing its sign at the integer fillings. However, the nature and degree of particle–hole asymmetry of the electronic structure at the transition points remain unexplored.

In this context, thermopower or the Seebeck effect is a unique tool to probe the particle–hole asymmetry of the electronic structure of MATBLG. Compared to electrical transport, it is relatively non-invasive as an open circuit voltage ($\Delta V$) is measured across the sample in the presence of a small temperature gradient ($\Delta T$) relative to the sample temperature. In the linear regime, using semi-classical Boltzmann transport theory and assuming energy-independent scattering time, the Seebeck coefficient ($S=-\Delta V/\Delta T$) can be written as $S=-(k_B/Te)[\int(\epsilon-\mu)g(\varepsilon)(-\mathrm{d}f/\mathrm{d}\varepsilon)\mathrm{d}\varepsilon]/[\int g(\varepsilon)(-\mathrm{d}f/\mathrm{d}\varepsilon)\mathrm{d}\varepsilon]$, where $e$, $T$, $\mu$, $g(\varepsilon)$ and $-\mathrm{d}f/\mathrm{d}\varepsilon$ are, respectively, the electronic charge, temperature, chemical potential, density of states and derivative of the Fermi function, and $k_B$ is the Boltzmann constant. It can be seen that the numerator is an odd function due to the $(\epsilon-\mu)$ term, and thus, the sign and magnitude of $S$ depend on the nature and extent of asymmetry of the density of states around the chemical potential, as shown schematically in Fig. 1. This figure depicts the expected thermopower for different band structures such as graphene, a semiconductor and a highly particle–hole-asymmetric band. Figure 1a shows the diffusion of electrons ($(\epsilon-\mu)>0$) and holes ($(\epsilon-\mu)<0$) from the hot end to the cold end. If the density of states is constant or symmetric with the energy around $\mu$, then the contributions from the electrons and holes cancel each other and $S$ vanishes. This can be seen in Fig. 1b, where for $\mu$ at the symmetric points such as the Dirac point and the van Hove singularities of graphene, and within the semiconducting bandgap, $S$ is zero. On the contrary, for a highly particle–hole-asymmetric band, the thermopower does not go to zero at zero energy (Fig. 1b), as the contribution from the hole band dominates over that from the electron band. As a result, $S$ is a highly sensitive probe to study the electronic structure around the transition points of MATBLG with cascaded transition. Moreover, MATBLG, with a superconducting dome

[1]Department of Physics, Indian Institute of Science, Bangalore, India. [2]National Institute for Materials Science, Tsukuba, Japan. [3]Max Planck Institute for the Physics of Complex Systems, Dresden, Germany. [4]These authors contributed equally: Arup Kumar Paul, Ayan Ghosh, Souvik Chakraborty. ✉e-mail: anindya@iisc.ac.in

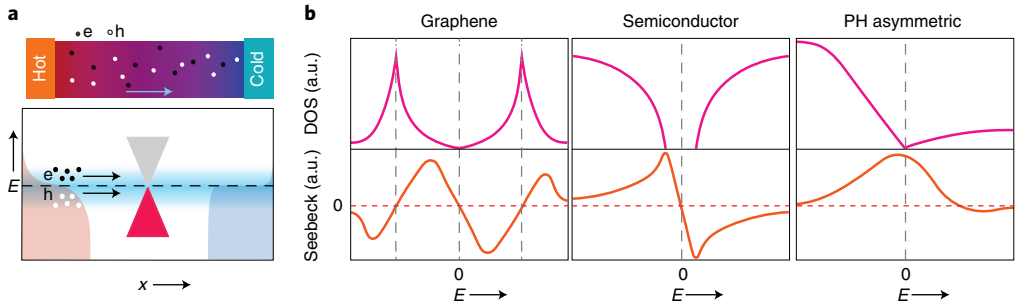


**Fig. 1 | Thermopower for different band structures. a**, Top: the diffusion of electrons and holes from the hot end to the cold end. Bottom: the contribution of electrons and holes to the chemical potential for a band with linear dispersion. The shaded regions correspond to the Fermi distributions of the hot and cold reservoirs. **b**, Top: a schematic of the density of states (DOS) for graphene (left), semiconductor (middle) and a highly particle–hole (PH)-asymmetric band (right) such as that near the Dirac revival of MATBLG. Bottom: the respective thermopowers, with several sign changes according to the semi-classical theory DOS and thermopower are shown in arbitrary units (a.u).

around half-filling, analogous to high-critical transition temperature ($T_c$) cuprate superconductors[3], is an ideal material to study the thermopower response around the superconducting transition[26].

Motivated by these observations, we have extensively explored the thermopower response of MATBLG and non magic-angle twisted bilayer graphene (TBLG) devices. Unlike previous work involving graphene and TBLG[27–34], we have utilized Johnson noise thermometry[35–38] to directly measure the temperature gradient across the MATBLG device and accurately determine $S$ across a temperature ranging from 100 mK to 10 K. Our measurements reveal an intricate dependence of $S$ on carrier density ($\nu$), temperature ($T$) and magnetic field ($B$). Our key observations are as follows. First, the measured thermopower at low temperatures deviates completely from the expected zero crossings, following the semi-classical Mott formula[39]. Instead, the thermopower exhibits peak-like features at all positive integer fillings including the Dirac point. Second, we observe a non-monotonic temperature dependence of the thermopower. The thermopower reaches a record high value of approximately 100 μV K$^{-1}$ at 1 K for half-filling of the conduction band. Third, we also observe unusually large peaks of $S \approx -(10–15)$ μV K$^{-1}$ at sub-kelvin temperatures around the superconducting transition, tracing the superconducting dome in the hole side, which completely vanishes at a small magnetic field of 0.1 T. We explain the first two results, showing emergent highly particle–hole-asymmetric densities of states at integer fillings, qualitatively using a simple model within self-consistent Hartree–Fock (HF) approximations. Furthermore, we discuss the plausible origins of the anomalous peaks around $T_c$. Our work highlights the ability of thermopower to independently provide unique insights into the novel quantum phenomena observed in MATBLG.

## Set-up and device response

Figure 2a shows a schematic of the devices and the measurement set-up for thermopower measurement. The devices consist of hexagonal boron nitride (hBN)-encapsulated TBLG on a Si/SiO$_2$ substrate. The details are described in Methods and Supplementary Section 1. For the thermopower measurement, an isolated gold heater line, as shown in Fig. 2a, is placed parallel to one side of the TBLG. To determine the thermopower or Seebeck coefficient ($S$), one needs to measure the generated thermoelectric voltage and the temperature difference ($\Delta T = T_h - T_c$, where $T_h$ and $T_c$ are the temperatures of the hot and cold contacts, respectively). We have utilized the well-established $2\omega$ lock-in technique[27–33] for measuring the thermoelectric voltage ($V_{2\omega}$) at $\omega = 13$ Hz. To measure $\Delta T$, we have utilized Johnson noise thermometry[35–38]. The details of the noise thermometry set-up can be found in our earlier work[35,40] and is also shown in Supplementary Section 3. The excess thermal noise, $S_V = 2k_B \Delta T R$, measured across the sample is used to determine $\Delta T$ (Supplementary Sections 6 and 7), where $R$ is the resistance of the device. Note that the above conversion between the excess thermal noise and $\Delta T$ is valid for a linear temperature profile. Any deviation from linearity may correct the coefficient keeping the proportionality relation between $S_V$ and $\Delta T$. To obtain the temperature profile in our device structure, in Supplementary Section 8 we have solved the three-dimensional Fourier heat-diffusion equation for the multilayer stack using finite element calculations with different parts of the device; Si/SiO$_2$ substrate, hBN flakes, metal contacts, TBLG and heater. The main finding is that the hBN plays a significant role in determining the almost linear temperature profile in our device structure. Figure 2c shows the measured $V_{2\omega}$ and $\Delta T$ as a function of the heater current at a bath temperature ($T$) of 1 K. In Fig. 2d, we plot $V_{2\omega}$ versus $\Delta T$ for MATBLG at different carrier densities ($n$). The linearity of the plots in Fig. 2d suggests that we are in the linear regime and the slope of each curve gives $S$ for a given $n$. We have measured $S$ from 100 mK to 10 K in the linear regime by adjusting the heater current such that $\Delta T$ always remains much smaller than $T$ (Supplementary Section 7). We have used three devices with approximate twist angles of 0.26, 1.05 and 1.86°.

The gate-dependent resistance ($R$) of MATBLG for different temperatures is shown in Fig. 2b. Here the gate voltage is replaced with an equivalent moiré filling factor, $\nu = 4n/n_s$, where $n$ is the carrier density induced by the gate voltage and $n_s$ is the carrier density required to fully fill the flat band (4 electrons/holes per moiré unit cell). As can be seen from the $R$ versus $\nu$ response, multiple resistance peaks appear at positive integer fillings, including the Dirac point, and these peak features survive up to 50 K and above. On the contrary, for negative filling, we see the prominent resistance peaks at $\nu = -4$ and between $\nu = -2$ and $\nu = -3$ where the resistance drops below 600 mK and saturates like a plateau at around 1.8 kΩ, showing the emergence of superconductivity. The above resistance arises due to two-probe geometry and gives an estimate of the contact resistance of the device. The resistance value at full filling ($\nu = \pm 4$) continuously decreases with increasing temperature. On the other hand, the resistance value at $\nu = 0$ and 2 decreases with increasing temperature up to ~10 K and then increases linearly, showing metallic nature (Supplementary Sections 11 and 12). Figure 2e and Fig. 2f plot the evolution of differential resistance ($\frac{dV}{dI}$) versus bias current ($I_{Bias}$) response with temperature and perpendicular magnetic field, respectively, at $\nu = -2.5$. These results confirm the existence of superconductivity, although the resistance is measured in two-probe geometry (Methods and Supplementary Section 14).

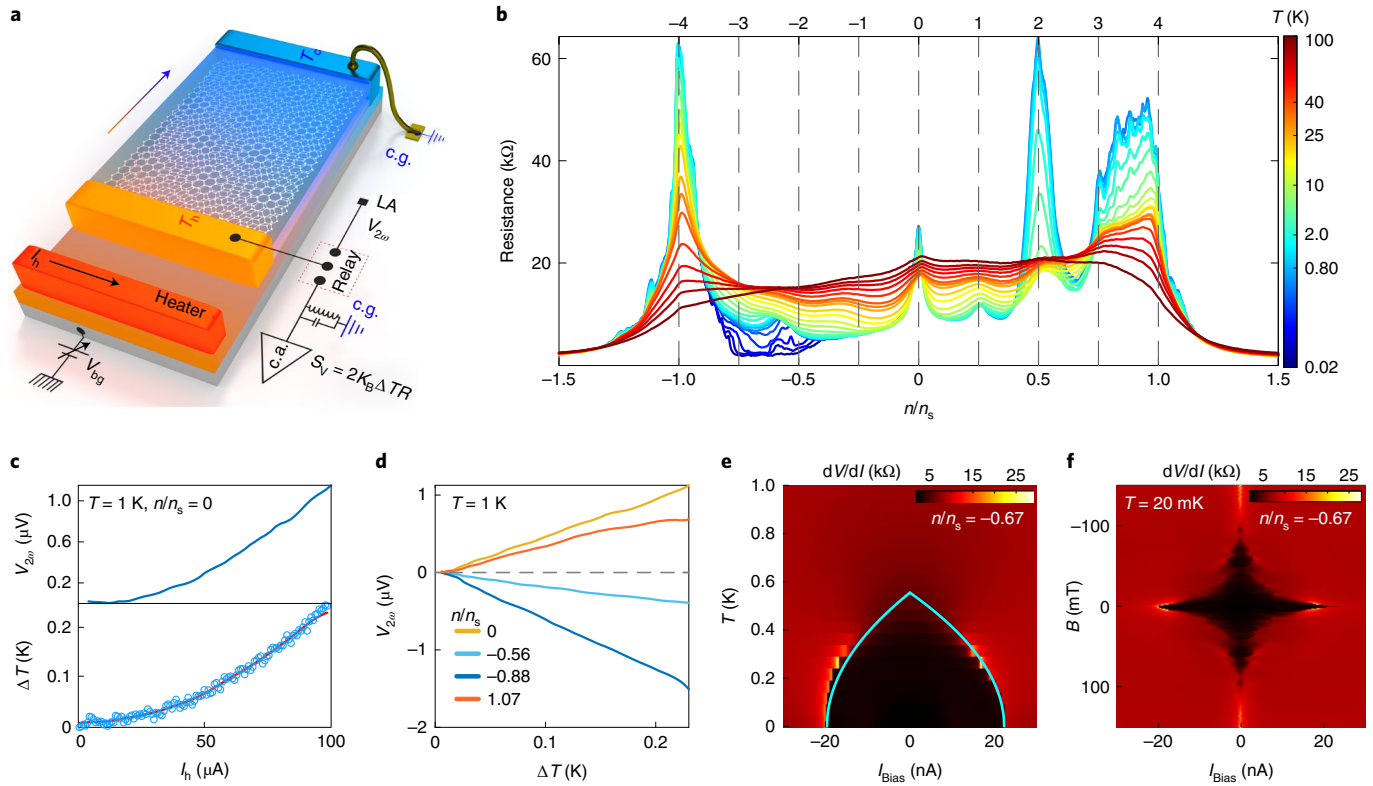


**Fig. 2 | Thermopower measurement set-up and device response. a**, Set-up of devices. Passing a current, $I_h$, through the heater creates the temperature gradient across the device, where the colder end is directly bonded to the cold ground (c.g.). The gate voltage, $V_{bg}$, controls the carrier density ($n$) of the device. The relay switches between the low-frequency and high-frequency measurement schemes. The low-frequency, $2\omega$ method, is used to measure the thermoelectric voltage ($V_{2\omega}$) at 13 Hz using the standard lock-in amplifier (LA) technique. The high-frequency (at 720 kHz) thermal noise ($S_V$) measurement consisting of an LC resonant tank circuit and cryo-amplifier (c.a.) is used to measure the temperature difference ($\Delta T$) across the device as $S_V = 2k_B\Delta TR$. **b**, Resistance versus filling fraction ($n/n_s$) as a function of increasing temperature, where $n_s$ is the carrier density required to fill the flat band. The top axis shows the number of electrons ($\nu$) per moiré lattice. The resistance peaks at the positive integer fillings ($\nu$) are visible at lower temperatures. At the hole side no such peaks are observed except at full filling. Below approximately 500 mK, the resistance drops to around 1.8 kΩ, within $n/n_s \approx -0.5$ to −0.75, which shows the emergence of superconductivity. **c**, Measured $V_{2\omega}$ (top) and $\Delta T$ (bottom) as a function of $I_h$ near the Dirac point at 1 K. **d**, $V_{2\omega}$ as a function of $\Delta T$ at 1 K, for different $n/n_s$, showing the linear response regime. The slope of each curve gives the value of $S$. **e**, Differential resistance ($dV/dI$) versus bias current ($I_{Bias}$) as a function of temperature, at $n/n_s \approx -0.67$, where critical current ($I_c$) is maximum. The dark region corresponds to the superconducting region. The sky blue solid line shows the theoretically generated $I_c$ using BCS theory, $I_c(T) = I_c(0)(1 - T/T_c)^2$, where $I_c(0)$ is the experimentally measured value at $T = 20$ mK. **f**, $dV/dI$ versus bias current ($I_{Bias}$) with increasing perpendicular magnetic field ($B_\perp$) at $n/n_s \approx -0.67$ and at around 20 mK. The dark black region corresponds to the superconducting region, which is absent at $B_\perp = 0.1$ T.

## Band reconstruction of MATBLG probed by thermopower

Figure 3a,b shows the measured thermopower versus $\nu$ at several temperatures from 200 mK to 10 K for MATBLG. At 10 K (Fig. 3a), the thermopower has approximate mirror symmetry for both conduction and valence bands, albeit with opposite signs. It can be seen that the thermopower changes its sign at the Dirac point, at flat-band full fillings ($\nu = \pm 4$) and around $\nu = \pm 1$. The sign of the thermopower depends on the type of carrier. It is positive for hole-like carriers and negative for electron-like carriers and its magnitude goes to zero at the symmetric points of the electronic structure, as described in Fig. 1 using the semi-classical equation. The density of states goes to zero symmetrically from both the conduction and valence bands, like at the Dirac point. Similarly, at the band full filling, with the energy gap between the flat and higher energy-dispersive bands, $S$ is expected to change sign. One more sign change is expected at the middle of the conduction or valence band as the single-particle density of states of the flat band reaches a maximum (van Hove singularity) around $\nu = \pm 2$. If the density of states is symmetric around the maxima, one would expect a sign change in $S$ exactly at $\nu = \pm 2$. However, the inherent asymmetry of the density of states of the conduction band or valence band, which is complex for MATBLG, can give rise to the sign change shift from $\nu = \pm 2$.

As we decrease the temperature below 10 K, the apparent asymmetry of $S$ (Fig. 3b) between the conduction and valence bands grows, similar to the asymmetry observed in the resistance data in Fig. 2b. Most importantly, the thermopower exhibits a positive peak around $\nu = 2$, and its magnitude increases rapidly with decreasing temperature and reaches a maximum value of the order of 95–100 μV K$^{-1}$ at 1 K, followed by a decrease of the magnitude with a further reduction of the temperature. Similarly, positive peaks are also seen around $\nu = 1$ and 3 at 3 K and at the Dirac point below 1 K. The observed positive peak in thermopower at the positive integer fillings, including the Dirac point, is quite striking. Any energy close to or greater than $k_BT$, either from the single-particle band structure or induced by electronic interactions, will give a sign change of $S$. In particular, one would expect $S$ to go to zero at the resistance maxima, that is, at the integer fillings given by the Mott formula[39] $S = (\pi^2 k_B T/3e)(\mathrm{d}\ln(R)/\mathrm{d}n)g(\epsilon)$, which gives zero at those points as shown in Fig. 3g for 0.2 K. Thus, one can see a complete violation of the Mott formula for MATBLG. The violation persists even up to 10 K, as shown in Supplementary Section 15. On the

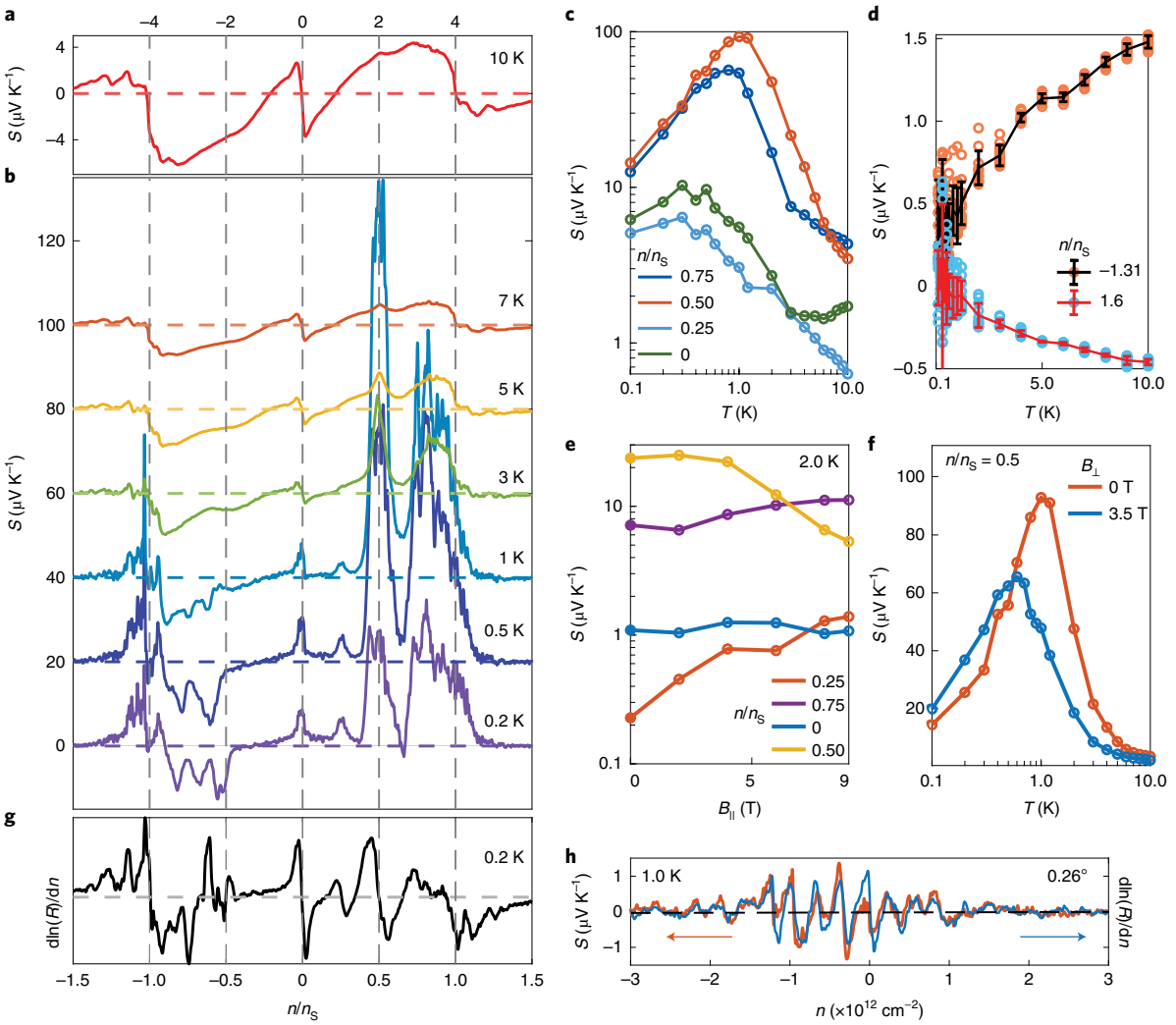


**Fig. 3 | Thermopower response at integer moiré fillings. a**, Measured thermopower of MATBLG with carrier fillings at 10 K. The horizontal dashed line corresponds to zero thermopower and the vertical dashed lines correspond to the integer number of electron fillings of the moiré lattice. **b**, Measured thermopower at several temperatures from 0.2 to 7 K. For clarity the data are shifted by 20 μV K$^{-1}$ along the *y* axis. The horizontal dashed lines are the zero thermopower for the corresponding temperatures. **c**,**d**, Temperature dependence of *S* for the flat band on a log–log scale at $n/n_s = 0$, 0.25, 0.50 and 0.75 (**c**) and for dispersive bands at the hole side ($n/n_s = -1.31$) and the electron side ($n/n_s = 1.6$) with a linear temperature scale (**d**). The open circles are the raw data and the solid lines trace the mean value. The error bars are the standard deviation. **e**, *S* versus $B_{\parallel}$ for a different thermal cycle at 2 K. **f**, *S* at half-filling versus temperature between zero and 10 K at $B_{\perp} = 0$ and 3.5 T. **g**, Derivative of resistance of MATBLG versus carrier density at 0.2 K according to the Mott formula. The horizontal dashed line corresponds to zero derivative. The clear sign changes at $\nu = 0, 1$ and 2 are seen but are absent in the *S* data in Fig. 3b. **h**, Measured *S* and derivative of resistance as function of carrier density (*n*) for a 0.26° non-magic angle TBLG device at 1 K. The qualitative agreement of sign changes between them can be seen.

contrary, for non magic-angle TBLG devices, the measured sign of *S* and the Mott formula match well, as shown in Fig. 3h for the 0.26° device (Supplementary Fig 19(a) for higher temperatures and Supplementary Fig. 19b for 1.86°).

The recurring thermopower peaks (Fig. 3b) at integer fillings with a positive sign (which usually occur for hole-like carriers) suggest, at least within an effective single-particle picture, repeated restructuring of the Fermi surface at integer fillings such that overall hole-like carriers are dominant. Pliable Fermi surfaces due to interactions around the integer fillings have been reported in MATBLG and Stoner like transitions[5,9,24,25] have been observed experimentally. The key features of these transitions are Lifshitz transition followed by a Dirac revival, which essentially gives rise to a large asymmetric density of states around the transition point such that, for $\nu > 0$, from one side (left side of the transition), the density of states rapidly drops whereas from the other side (right side of the transition) the density of states increases gradually, similar to a sawtooth. Such an asymmetric density of states can give rise to a large value of *S* around the transition point as shown in Fig. 1 and we have discussed this in detail in the theoretical section. It can be seen from Fig. 3h and Supplementary Section 15 that, for non magic-angle devices, we do not observe any thermopower peaks and the measured *S* is around 1 μV K$^{-1}$ at 1 K as expected for graphene-based devices at such low temperatures[27–29].

The temperature dependence of *S* for different integer fillings, including the Dirac point, is shown in Fig. 3c. The common key feature is the non-monotonic temperature dependence of *S* with a maximum at a certain temperature, which depends on the filling. For example, at $\nu = 2$ and 3 the peak appears around 1 K, whereas it is around 0.3 K for $\nu = 1$ and the Dirac point. The deviation from the linear *T* dependence of *S* again suggests the strong violation of Mott's formula[39] for the flat band of MATBLG. Figure 3d shows

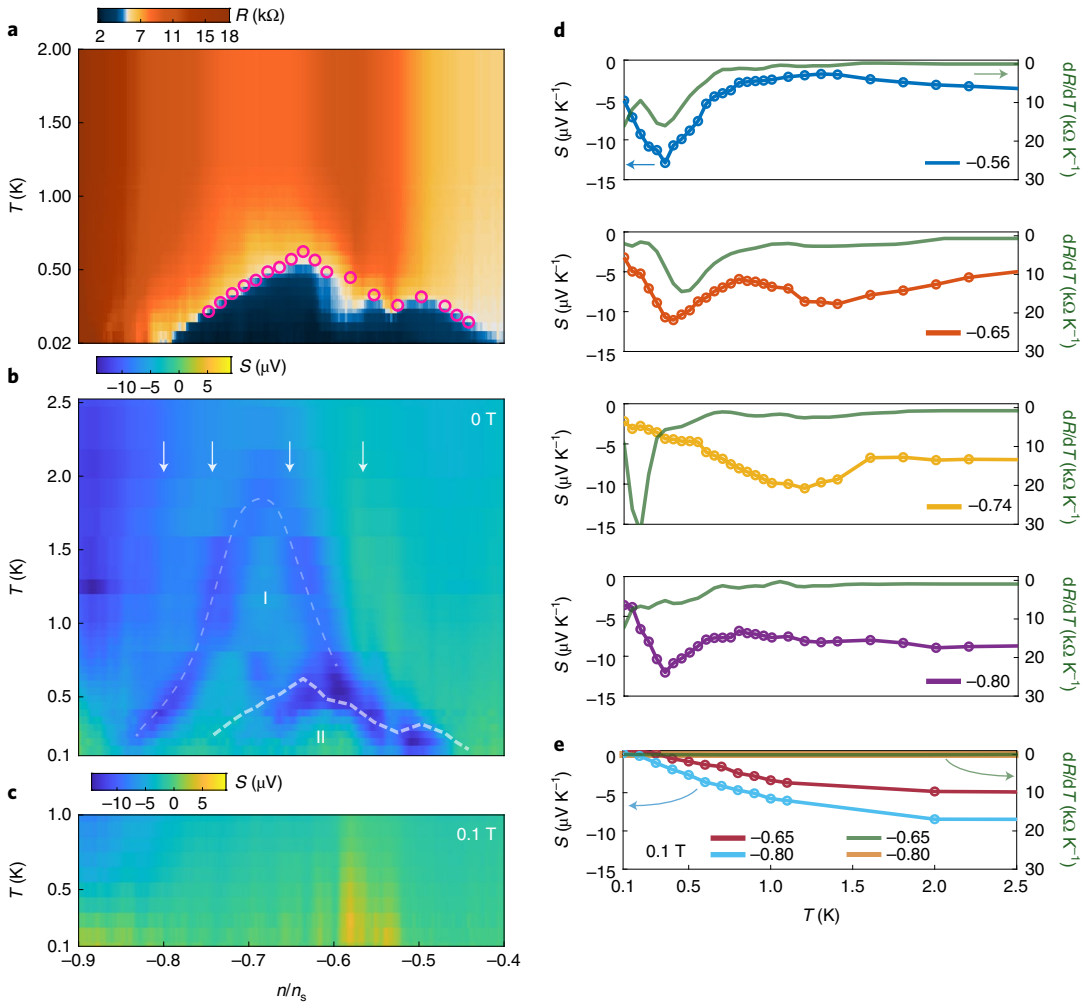


**Fig. 4 | Thermopower across the superconducting transition. a**, Two-dimensional colour map of resistance as a function of temperature and carrier filling for the hole-side flat band of MATBLG. The dark blue portion corresponds to the superconducting region around the weaker Mott peak at $n/n_s \approx -0.55$. The open circles are the $T_c$ at different carrier densities as determined from the differential resistance versus critical current plot as a function of temperature as shown in Fig. 2e. **b**, Two-dimensional colour map of measured thermopower as a function of temperature and carrier filling. The dark blue portions are the negative thermopower peaks as shown as the cut lines in **d** for the carrier densities marked by the white vertical arrows. Regions I and II correspond to two different dome-like portions, where region II matches well with the superconducting dome seen in **a** as shown by the white dashed line, which is the trace of $T_c$ as shown in **a**. The other white dashed line enclosing region I is the guiding line. **c**, The measured thermopower at a $B_\perp = 0.1$ T without peak-like features in $S$. **d**, Open circles with connected lines in different panels are the cut lines of measured $S$ as a function of temperature from **b** at $n/n_s = -0.56, -0.65, -0.74$ and $-0.80$. The solid lines are the corresponding cut lines of $dR/dT$ from **a**. **e**, Thermopower cut lines for $B_\perp = 0.1$ T at $n/n_s = -0.65$ and $-0.80$ and the corresponding $dR/dT$.

the variation of $S$ for the dispersive band with temperature. Here, considering the relatively smaller magnitude of $S$ in the dispersive band, we have shown the mean thermopower within a density range of $\nu \pm 0.1\nu$ (10 data points around $n/n_s \approx 1.6$ and $n/n_s \approx -1.31$) as function of temperature, with the error bars representing standard deviations around the mean values. The open circles are the individual data points and the solid lines trace the mean value. It can be seen from Fig. 3d that below 1 K, the fluctuations in mesoscopic nature[27] dominate. However, above 1 K, it can be clearly seen that the measured $S$ in the dispersive bands increases monotonically with increasing temperature and shows almost close to linear increment for $n/n_s \approx 1.6$ and $n/n_s \approx -1.31$, consistent with the Mott formula. Furthermore, the response of $S$ with the in-plane magnetic field ($B_\parallel$) underlies the nature of the ground states at different integer fillings. As can be seen in Fig. 3e (for a different thermal cycle as shown in Supplementary Section 16) the thermopower peaks increase with $B_\parallel$ at $\nu = 1$, but decrease at $\nu = 2$. These observations are consistent with the cascade of Dirac revival picture in ref. [25], where the emergence of flavoured symmetry breaking in MATBLG with a polarized ground state at $\nu = 1$ strengthens the transition and thus makes a more particle–hole-asymmetric density of states resulting in higher $S$. At $\nu = 2$ the value of $S$ also decreases with $B_\perp$, as shown as a function of $T$ in Fig. 3f (see also Supplementary Section 16). It can be seen that the peak position of $S$ is shifted to lower temperatures around 0.6 K at $B_\perp = 3.5$ T with a value of around 70 μV K$^{-1}$. It should be noted that the $S$ of the dispersive band and non magic-angle TBLG devices remain insensitive to $B_\parallel$ (Supplementary Section 16). Note that in Supplementary Section 13 we have also discussed the accuracy of our thermopower measurement.

## Anomalous thermopower response around the superconducting dome

As shown in Fig. 3b, there are no thermopower peaks for the valence flat band of the MATBLG device in the temperature range 2–10 K.

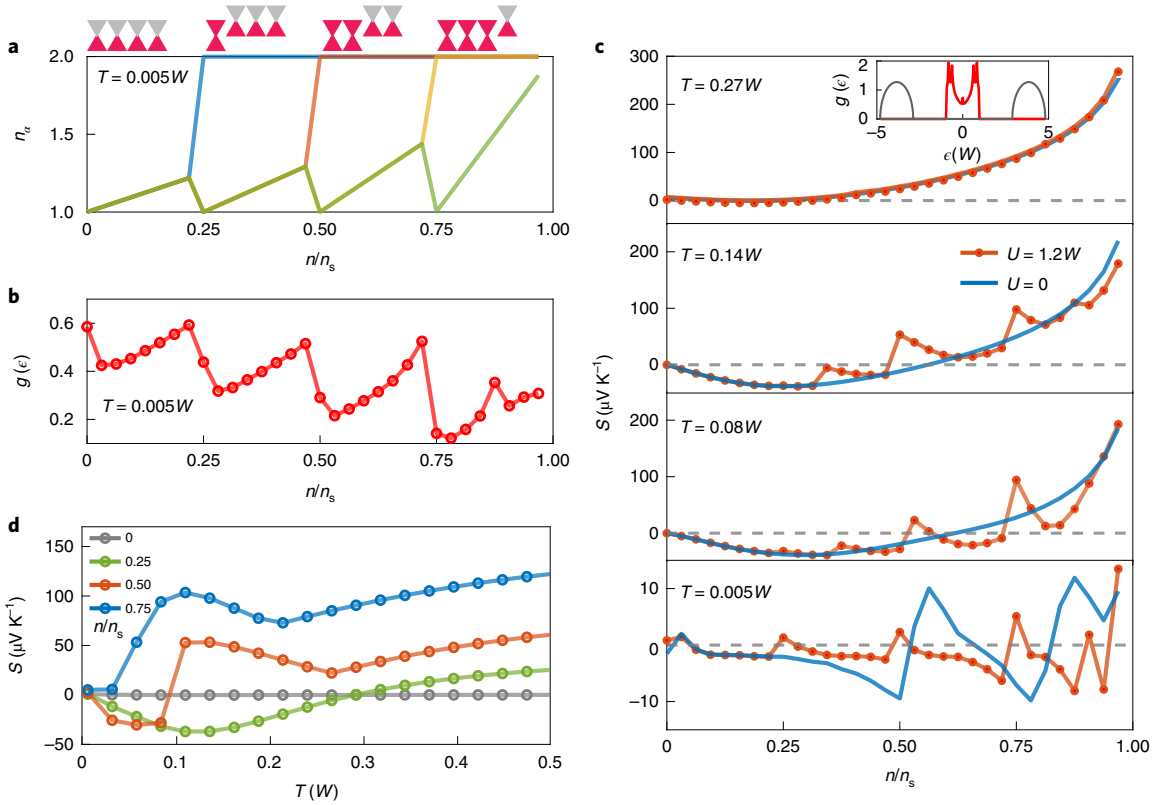


**Fig. 5 | Cascade of Dirac revivals and thermopower peaks around integer fillings. a**, The occupation ($n_\alpha, \alpha = 1, \ldots, 4$) of individual flavours as a function of filling $n/n_s$, obtained from HF calculations for $T = 0.005W$ and a local inter-flavour interaction $U = 1.2W$. At zero filling, the Dirac cones corresponding to the four spin-valley degrees of freedom are degenerate. A cascade of Stoner-like transitions close to the integer fillings leads to complete filling of one, two and three of the flavours successively while the filling of the remaining flavour(s) resets to the Dirac point. **b**, The resultant HF density of states $g(\epsilon)$ at the chemical potential at $T = 0.005W$ exhibits the sawtooth feature. The effective single-particle density of states $g(\epsilon)$ changes drastically at each integer filling and shows strong low-energy particle–hole asymmetry (Supplementary Fig. 25). **c**, The calculated thermopower $S$ in the HF approximation (red circles with lines) shows peak-like features around the integer fillings due to the Dirac revivals (**a**). The top to bottom panels are in the order of decreasing temperature $T = 0.27W, 0.14W, 0.08W$ and $0.005W$. The thermopower $S_0$ obtained using a 'rigid' non-interacting single particle density of states (top, inset) is shown by solid blue lines. The non-interacting $S_0$ exhibits one sign change around the half-filling for higher temperatures $T \gtrsim 0.08W$ and multiple sign changes across the two van Hove singularities of the non-interacting density of states at very low temperature (bottom), but these peaks depend on the details of the non-interacting density of states and are not necessarily tied to integer the fillings, unlike $S(\nu)$ in the interacting cases. **d**, Non-monotonic temperature dependence of thermopower at integer fillings from the cascaded transitions. The Dirac-revived symmetry-broken state at $n/n_s = 0.50$ only gets stabilized at finite temperature for the particular non-interacting density of states, as indicated by a sign change in $S$ around $T \simeq 0.1W$.

This is consistent with the weaker cascaded transitions observed for the hole side in ref. [25]. It was shown that a larger twist angle close to 1.1° is required to observe the sawtooth behaviour in the density of states for the hole side. However, for the MATBLG device, some peak-like features are developed within $\nu \approx -2$ to $-3.5$ below 2 K. The number of peaks and their positions in filling change with decreasing temperature; one weak negative peak is seen at 2 K, whereas three prominent negative peaks are observed at 0.2 K. Figure 4a shows the two-dimensional (2D) colour map of the resistance with temperature and filling. The darker blue region corresponds to the superconducting phase seen close to a weak resistance peak at $n/n_s \approx -0.55$ (details in Supplementary Section 14). The open circles denote superconducting transition temperature $T_c$ as a function of filling, obtained from critical current measurements shown in Fig. 2e and Supplementary Section 14.

Figure 4b shows the corresponding 2D colour map of $S$ at zero magnetic field. Here the darker blue shaded ribbons enclosing dome-like structures correspond to negative thermopower peaks. A closer view shows two inter-penetrating dome-like structures marked by dashed white lines and labelled as I and II in Fig. 4b. The dashed white line enclosing region II is the trace of $T_c$ as shown in Fig. 4a, whereas the white dashed line enclosing region I is a guide to the eye to follow the locus of the broad negative thermopower peaks. As evident from Fig. 4a,b, there are clear resemblances between the peak position in $S$ enclosing region II and the $T_c(n)$ dome. This can be further ascertained from Fig. 4d, where $S$ from Fig. 4b and $\mathrm{d}R/\mathrm{d}T$ for Fig. 4a are plotted as a function of $T$ for fixed fillings, $n/n_s = -0.56$ and $-0.65$. Both $S$ and $\mathrm{d}R/\mathrm{d}T$ exhibit prominent peaks around $T_c$. However, the peak in $S$ enclosing region I in Fig. 4b has hardly any direct correspondence to the resistance data in Fig. 4a, as can be seen in Fig. 4d, where $S(T)$ exhibits broad peaks at $n/n_s = -0.74$ and $-0.80$, but $\mathrm{d}R/\mathrm{d}T$ does not show any such feature around the same temperature.

Apart from the correlation between the locus of the thermopower peak in the $n$–$T$ plane and $T_c(n)$ over a large part of the superconducting dome, a clue to the possible origin of the unusual thermopower peak is obtained by applying a $B_\perp$. As shown in Fig. 4c, the peak in $S$ around region II completely disappears with the application of a tiny $B_\perp = 0.1$ T. This is demonstrated in Fig. 4e by plotting $S(T)$ for $n/n_s = -0.65$ and $-0.8$, together with the corresponding $\mathrm{d}R/\mathrm{d}T$. These observations suggest that the anomalous peak in $S$ in Fig. 4b, particularly enclosing region II, may have a connection

to the superconductivity of MATBLG. The observed anomalous thermopower peak around $T_c$ is quite striking. Anomalously large thermopower response around $T_c$, and even extending far above $T_c$, has been reported in the transverse thermoelectric coefficient, that is the Nernst coefficient[26], for high-$T_c$ cuprate superconductors. However, experimental observations of peaks in the longitudinal component of $S$ are scarce[41]. Such thermopower peaks have been theoretically predicted[41,42] to exist above, albeit close to, $T_c$ from superconducting fluctuations under certain situations, for example for a superconductor in the dirty limit[41,42]. The observed thermopower in our MATBLG device may have a similar origin, as disorder due to twist-angle inhomogeneity[25,43] is naturally present in the system. In Supplementary Section 14, we have discussed the various plausible origins for observing the anomalous peaks around $T_c$. At present, the superconducting fluctuations at the dirty limit are the most plausible explanation. However, future studies, for example on the Nernst effect, will be important to unravel the actual mechanism in MATBLG. The origin of the broader peak enclosing region I remains unclear and will be an exciting direction for future studies.

## Emergent low-energy particle–hole asymmetry and giant thermopower peaks

As already mentioned, the thermopower peaks suggest strong emergent low-energy particle–hole asymmetry of the putative correlated states at integer fillings, at least, within the effective single-particle or HF descriptions of various possible symmetry-broken states[44–46]. As discussed in Methods and Supplementary Section SI, we use a simple minimal model[25] with four fermionic flavours, corresponding to the spin and valley degrees of freedom, each described in terms of a single-particle density of states[1,25,47] and interacting via a local Coulomb interaction. We treat the latter using the self-consistent HF approximation and use the resulting HF density of states to calculate the resistivity and thermopower as a function of filling and temperature, using the Kubo formulae (Supplementary Section 19). We have used different non-interacting densities of states, obtained from both effective continuum models[1,47], with and without lattice relaxation effects[47], as well as a tight-binding model[48] (Supplementary Section 19). The main results are summarized in Fig. 5, where the peak value of $S$ reaches around 50–100 $\mu$V K$^{-1}$ for $\nu \simeq 2$ and 3 at $T \simeq 0.1W$, consistent with our experimental observations (Fig. 3b). The temperature range $T \simeq 0.005$–$0.27W$ corresponds to 200 mK–13 K, for a bandwidth $2W \simeq 10$ meV. For comparison, in Fig. 5c (solid blue lines), we have shown $S_0$ for the non-interacting case (see Fig. 5c caption for details). We find the thermopower peak around an integer filling to be a robust feature whenever the Dirac revival is stabilized within the HF approximation. This result supports the simultaneous presence of thermopower (Fig. 3b) and resistance (Fig. 2b) peaks, as well as the non-monotonic temperature dependence of $S$ (Fig. 3c) in our experiment.

## Discussion

Our theory qualitatively captures the thermopower peaks, but $S(n)$ follows an overall 'background' profile dictated by the non-interacting $S_0(n)$ (Fig. 5c) and its sign change around half-filling. There could be several reasons behind the deviation of $S$ obtained from the HF approximation compared to the experimental one. For example, effects of more complex and realistic single-particle density of states for MATBLG than the used continuum model[1,25,47], twist angle inhomogeneity[25,43] and strong correlations in the strange metal state[49] (see Supplementary Section 19 for a detailed discussion). Moreover, we should note that there are theoretical models[44–46] which lead to a small gap ($\Delta$) at the Dirac revivals. This will be consistent with the simultaneous presence of thermopower and resistance peaks at integer fillings provided $k_B T \gtrsim \Delta$. At much lower temperatures, $S$ is expected to change sign across the position of the resistance peak. Thus, our thermopower results put a tighter upper bound, $\Delta \approx 0.1$–$0.2$ meV (activation gap in Supplementary Section 12), on the correlation-induced gap at integer fillings. In Supplementary Section 19, we also discuss the expected thermopower from various other kinds of ground state, such as Chern insulators[50], the isospin Pomeranchuk effect[19,20] and phonon drag[27], in detail. Although Chern insulators with a large gap cannot give rise to thermopower peaks at low temperature, the Pomeranchuk effect can lead to extra entropy and thus can enhance the thermopower at integer fillings. The phonon drag is expected to be negligible below 10 K, which has been previously seen for monolayer and bilayer graphene[27].

## Online content

Any methods, additional references, Nature Research reporting summaries, source data, extended data, supplementary information, acknowledgements, peer review information; details of author contributions and competing interests; and statements of data and code availability are available at https://doi.org/10.1038/s41567-022-01574-3.

Received: 10 September 2021; Accepted: 25 February 2022;
Published online: 21 April 2022

## References

1. Bistritzer, R., & MacDonald, A. H. Moiré bands in twisted double-layer graphene. *Proc. Natl Acad. Sci. USA* **108**, 12233–12237 (2011).
2. Cao, Y. et al. Correlated insulator behaviour at half-filling in magic-angle graphene superlattices. *Nature* **556**, 80–84 (2018).
3. Cao, Y. et al. Unconventional superconductivity in magic-angle graphene superlattices. *Nature* **556**, 43–50 (2018).
4. Yankowitz, M. et al. Tuning superconductivity in twisted bilayer graphene. *Science* **363**, 1059–1064 (2019).
5. Wu, S., Zhang, Z., Watanabe, K., Taniguchi, T. & Andrei, E. Y. Chern insulators, van Hove singularities and topological flat bands in magic-angle twisted bilayer graphene. *Nat. Mater.* **20**, 488–494 (2021).
6. Saito, Y., Ge, J., Watanabe, K., Taniguchi, T. & Young, A. F. Independent superconductors and correlated insulators in twisted bilayer graphene. *Nat. Phys.* **16**, 926–930 (2020).
7. Lu, X. et al. Superconductors, orbital magnets and correlated states in magic-angle bilayer graphene. *Nature* **574**, 653–657 (2019).
8. Arora, H. S. et al. Superconductivity in metallic twisted bilayer graphene stabilized by $WSe_2$. *Nature* **583**, 379–384 (2020).
9. Park, J. M., Cao, Y., Watanabe, K., Taniguchi, T. & Jarillo-Herrero, P. Tunable strongly coupled superconductivity in magic-angle twisted trilayer graphene. *Nature* **590**, 249–255 (2021).
10. Sharpe, A. L. et al. Emergent ferromagnetism near three-quarters filling in twisted bilayer graphene. *Science* **365**, 605–608 (2019).
11. Das, I. et al. Symmetry-broken Chern insulators and Rashba-like Landau-level crossings in magic-angle bilayer graphene. *Nat. Phys.* **17**, 710–714 (2021).
12. Nuckolls, K. P. et al. Strongly correlated Chern insulators in magic-angle twisted bilayer graphene. *Nature* **588**, 610–615 (2020).
13. Choi, Y. et al. Correlation-driven topological phases in magic-angle twisted bilayer graphene. *Nature* **589**, 536–541 (2021).
14. Stepanov, P. et al. Competing zero-field Chern insulators in superconducting twisted bilayer graphene. *Phys. Rev. Lett.* **127**, 197701 (2021).
15. Pierce, A. T. et al. Unconventional sequence of correlated Chern insulators in magic-angle twisted bilayer graphene. *Nat. Phys.* **17**, 1210–1215 (2021).
16. Serlin, M. et al. Intrinsic quantized anomalous Hall effect in a moiré heterostructure. *Science* **367**, 900–903 (2020).
17. Jiang, Y. et al. Charge order and broken rotational symmetry in magic-angle twisted bilayer graphene. *Nature* **573**, 91–95 (2019).
18. Cao, Y. et al. Nematicity and competing orders in superconducting magic-angle graphene. *Science* **372**, 264–271 (2021).
19. Rozen, A. et al. Entropic evidence for a Pomeranchuk effect in magic-angle graphene. *Nature* **592**, 214–219 (2021).
20. Saito, Y. et al. Isospin Pomeranchuk effect in twisted bilayer graphene. *Nature* **592**, 220–224 (2021).
21. Choi, Y. et al. Electronic correlations in twisted bilayer graphene near the magic angle. *Nat. Phys.* **15**, 1174–1180 (2019).
22. Xie, Y. et al. Spectroscopic signatures of many-body correlations in magic-angle twisted bilayer graphene. *Nature* **572**, 101–105 (2019).
23. Kerelsky, A. et al. Maximized electron interactions at the magic angle in twisted bilayer graphene. *Nature* **572**, 95–100 (2019).

24. Wong, D. et al. Cascade of electronic transitions in magic-angle twisted bilayer graphene. *Nature* **582**, 198–202 (2020).
25. Zondiner, U. et al. Cascade of phase transitions and Dirac revivals in magic-angle graphene. *Nature* **582**, 203–208 (2020).
26. Xu, Z. A., Ong, N. P., Wang, Y., Kakeshita, T. & Uchida, S. Vortex-like excitations and the onset of superconducting phase fluctuation in underdoped $La_{2-x}Sr_xCuO_4$. *Nature* **406**, 486–488 (2000).
27. Zuev, Y. M., Chang, W. & Kim, P. Thermoelectric and magnetothermoelectric transport measurements of graphene. *Phys. Rev. Lett.* **102**, 096807 (2009).
28. Checkelsky, J. G. & Ong, N. P. Thermopower and Nernst effect in graphene in a magnetic field. *Phys. Rev. B* **80**, 081413 (2009).
29. Nam, S.-G., Ki, D.-K. & Lee, H.-J. Thermoelectric transport of massive Dirac fermions in bilayer graphene. *Phys. Rev. B* **82**, 245416 (2010).
30. Wang, C.-R. et al. Enhanced thermoelectric power in dual-gated bilayer graphene. *Phys. Rev. Lett.* **107**, 186602 (2011).
31. Duan, J. et al. High thermoelectricpower factor in graphene/hBN devices. *Proc. Natl Acad. Sci. USA* **113**, 14272–14276 (2016).
32. Ghahari, F. et al. Enhanced thermoelectric power in graphene: violation of the Mott relation by inelastic scattering. *Phys. Rev. Lett.* **116**, 136802 (2016).
33. Mahapatra, P. S. et al. Misorientation-controlled cross-plane thermoelectricity in twisted bilayer graphene. *Phys. Rev. Lett.* **125**, 226802 (2020).
34. Ghawri, B. et al. Breakdown of semiclassical description of thermoelectricity in near-magic angle twisted bilayer graphene. *Nat. Commun.* **13**, 1522 (2022).
35. Srivastav, S. K. et al. Universal quantized thermal conductance in graphene. *Sci. Adv.* **5**, eaaw5798 (2019).
36. Fong, K. C. & Schwab, K. Ultrasensitive and wide-bandwidth thermal measurements of graphene at low temperatures. *Phys. Rev. X* **2**, 031006 (2012).
37. Crossno, J. et al. Observation of the Dirac fluid and the breakdown of the Wiedemann-Franz law in graphene. *Science* **351**, 1058–1061 (2016).
38. Betz, A. C. et al. Supercollision cooling in undoped graphene. *Nat. Phys.* **9**, 109–112 (2013).
39. Cutler, M. & Mott, N. F. Observation of Anderson localization in an electron gas. *Phys. Rev.* **181**, 1336–1340 (1969).
40. Srivastav, S. K. et al. Vanishing thermal equilibration for hole-conjugate fractional quantum Hall states in graphene. *Phys. Rev. Lett.* **126**, 216803 (2021).
41. Howson, M. A., Salamon, M. B., Friedmann, T. A., Rice, J. P. & Ginsberg, D. Anomalous peak in the thermopower of $YBa_2Cu_3O_{7-\delta}$ single crystals: a possible fluctuation effect. *Phys. Rev. B* **41**, 300–306 (1990).
42. Lu, Y. & Patton, B. R. Fluctuation thermopower above the superconducting transition temperature. *J. Phys. Condens. Matter* **7**, 9247–9254 (1995).
43. Uri, A. et al. Mapping the twist-angle disorder and Landau levels in magic-angle graphene. *Nature* **581**, 47–52 (2020).
44. Po, H. C., Zou, L., Vishwanath, A. & Senthil, T. Origin of Mott insulating behavior and superconductivity in twisted bilayer graphene. *Phys. Rev. X* **8**, 031089 (2018).
45. Bultinck, N. et al. Ground state and hidden symmetry of magic-angle graphene at even integer filling. *Phys. Rev. X* **10**, 031034 (2020).
46. Shavit, G., Berg, E., Stern, A. & Oreg, Y. Theory of correlated insulators and superconductivity in twisted bilayer graphene. *Phys. Rev. Lett.* **127**, 247703 (2021).
47. Koshino, M. et al. Maximally localized Wannier orbitals and the extended Hubbard model for twisted bilayer graphene. *Phys. Rev. X* **8**, 031087 (2018).
48. Moon, P. & Koshino, M. Energy spectrum and quantum Hall effect in twisted bilayer graphene. *Phys. Rev. B* **85**, 195458 (2012).
49. Cao, Y. et al. Strange metal in magic-angle graphene with near Planckian dissipation. *Phys. Rev. Lett.* **124**, 076801 (2020).
50. Andrei, E. Y. & MacDonald, A. H. Graphene bilayers with a twist. *Nat. Mater.* **19**, 1265–1275 (2020).

## Methods

**Device fabrication and measurement scheme.** The devices consist of hBN encapsulated TBLG on a Si/$SiO_2$ substrate. The typical length and width of the devices are 6 μm and 2 μm, respectively. The usual 'tear and stack' technique[2,3] is used to fabricate the devices and is described in detail in Supplementary Section 1. For the resistance measurement, we employ the low-frequency (13 Hz) lock-in technique (Supplementary Section 3). For the thermopower measurement, an isolated gold line, as shown in Fig. 2a, is placed parallel to one side of the TBLG at a separation of 3 μm. Passing a current ($I_h$) through the heater creates a temperature gradient across the length of the TBLG as depicted by the colour gradient (red to blue) in Fig. 2a. As a result, the contact near to the heater will be hotter ($T_h$) compared with the far contact ($T_c$). The temperature of the far contact ($T_c$) is maintained at the bath temperature of the cryo-free dilution fridge by directly anchoring it to the cold finger attached to the mixing chamber plate, which we call a cold ground (c.g.). To measure $\Delta T$, we have utilized Johnson noise thermometry. As shown in Fig. 2a, the thermometry circuit consists of an LC resonant ($f_r \approx 720$ kHz) tank circuit, followed by a cryogenic amplifier (c.a.). The relay sitting at the mixing chamber plate (Fig. 2a) is used to switch between the thermoelectric voltage and temperature measurement.

**Activation gaps, bandwidth and superconducting transition temperature of MATBLG.** The value of the resistance at full filling ($\nu = \pm 4$) continuously decreases with increasing temperature up to much higher $T \sim 100$ K. On the other hand, the value of the resistance at $\nu = 0$ and 2 decreases with increasing temperature up to ≈10 K and then increases linearly, showing metallic nature (Supplementary Section 11). These observations are consistent with earlier reports for MATBLG[2–9]. The gaps ($\Delta$) determined from the activated plot for $\nu = 0$, 2 and ±4 are, respectively, around 0.05, 0.25, 11.5 and 9.25 meV as shown in Supplementary Sections 11 and 12. Furthermore, it can be seen (Supplementary Section 11) that there is a crossover from metallic nature to insulating nature at a higher temperature due to interband excitation of the carriers between the flat and dispersive bands. From the crossover temperature, at around 150 K (around the Dirac point), one can estimate the bandwidth ($2W$) and this was found to be of the order of 10 meV for MATBLG. In Fig. 2e,f, we have shown the differential resistance versus bias current with temperature and perpendicular magnetic field around the superconducting dome. To extract the transition temperature at a given filling, we compare the experimental data with the theoretically generated critical current versus temperature using Bardeen–Cooper–Schreiffer (BCS) theory, $I_c(T) = I_c(0)(1 - T/T_c)^2$, where $I_c(0)$ is the experimentally measured critical current at $T = 20$ mK, and vary $T_c$ such that the theoretically generated $I_c(T)$ traces the experimentally measured $I_c$ in Fig. 2e. This was repeated for other carrier densities and is shown in Supplementary Section 14. The extracted critical temperature was found to be around 500 mK at $\nu \approx -2.5$ (Supplementary Section 14). The measured value of $T_c$ and critical field ($B_c \approx 100$ mT) of our device matches reasonably well with the available data for MATBLG[3,4,6–9]. Note that the Fraunhofer-like pattern in Fig. 2f can be explained by the interference between percolating superconducting paths separated by the normal islands, which is a generic feature in MATBLG due to twist-angle inhomogeneity[9,25,43]. These patterns further establish the existence of the superconductivity in our device, although the measurement was carried out in two-probe geometry.

**Theory.** As discussed in detail in Supplementary Section 19, we compute the thermopower and resistivity as a function of filling and temperature for the model of ref. [25] using the HF approximation. The model consists of four spin-valley flavours, interacting with local Coulomb interaction $U$. For the results reported in the main text, we have taken $U = 1.2W$, where $W$ is the band width of the conduction (valence) band. The HF self-consistency equations depend on the non-interacting density of states of the moiré flat bands. We use various non-interacting densities of states, for example densities of states obtained from the continuum Bistritzer–MacDonald model[1] in ref. [25] and the density of states generated from the continuum model of ref. [47], which includes lattice relaxation effects. The self-consistent HF density of states is then used to compute thermopower and resistivity using the Kubo formulae, neglecting vertex corrections. We assume a constant band velocity and use a small impurity scattering rate $\Gamma_0 = 0.001W$ in the Kubo formulae.

## Data availability

Source data are provided with this paper. Additional information related to this work is available from the corresponding author upon reasonable request.

## Acknowledgements

A.D. thanks the Department of Science and Technology (DST) and SERB (DSTO-2051), India for financial support and the MHRD, Government of India under STARS research funding (STARS/APR2019/PS/156/FS), IRPHA(IPA/2020/000034) and also acknowledges the Swarnajayanti Fellowship of the DST/SJF/PSA-03/2018-19. K.W. and T.T. acknowledge support from the Elemental Strategy Initiative conducted by the MEXT, Japan and the CREST (JPMJCR15F3), JST.

## Author contributions

S.C., A.K.P. and U.R. contributed to device fabrication. A.G. and A.K.P. contributed to data acquisition and analysis. R.D. contributed to initial measurements. A.D. contributed to conceiving the idea and designing the experiment, data interpretation and analysis. K.W. and T.T. synthesized the hBN single crystals. A.P., A.A., S.M. and S.B. contributed to development of theory and data interpretation. All the authors contributed to writing the manuscript.

## Competing interests

The authors declare no competing interests.

## Additional information

**Supplementary information** The online version contains supplementary material available at https://doi.org/10.1038/s41567-022-01574-3.

**Correspondence and requests for materials** should be addressed to Anindya Das.

**Peer review information** *Nature Physics* thanks Petr Stepanov, Yuanping Chen and the other, anonymous, reviewer(s) for their contribution to the peer review of this work.

**Reprints and permissions information** is available at www.nature.com/reprints.